

# Corrosion protection of Mg-SiC nanocomposite through plasma electrolytic oxidation coating process

Ali P. Golhin<sup>1,2</sup> | Sepideh Kamrani<sup>1</sup>  | Claudia Fleck<sup>1</sup> | Alireza Ghasemi<sup>1</sup> 

<sup>1</sup>Department of Materials Science & Engineering, Institute of Technology Berlin, Berlin, Germany

<sup>2</sup>Department of Manufacturing and Civil Engineering, Norwegian University of Science and Technology, Gjøvik, Norway

## Correspondence

Alireza Ghasemi, Department of Materials Engineering, Institute of Technology Berlin, Str. des 17. Juni 135-Sekr. EB 13, Berlin 10623, Germany.  
Email: [ghasemi@yahoo.com](mailto:ghasemi@yahoo.com)

## Funding information

None

## Abstract

Understanding the role of nanoparticles in magnesium (Mg)-based materials and protective coating provides valuable information to achieve an optimized combination of mechanical and corrosion protection properties of Mg nanocomposites. The present study investigates the effects of SiC nanoparticles on the corrosion behavior and structure of Mg-SiC composites substrates coated by plasma electrolytic oxidation (PEO). Moreover, the influence of different volume fractions of SiC<sub>n</sub> up to 10% on corrosion behavior and galvanic reactions between Mg matrix and SiC particles was also investigated. The morphology, distribution of the phases, and the microstructure of the coating were characterized by SEM, EDAX, X-ray photoelectron spectroscopy, and XRD. The corrosion resistance of the samples was determined through dynamic polarization and electrochemical impedance spectroscopy tests before and after PEO coating treatment. The results indicate that the Mg nanocomposite with 1 vol% SiC<sub>n</sub> (M1Sn) coated by PEO coating shows higher corrosion resistance than the samples with a higher percentage of SiC<sub>n</sub>, as well as the sample without SiC<sub>n</sub> particles.

## KEYWORDS

corrosion, mechanical milling, Mg-SiC nanocomposite, plasma electrolytic oxidation, powder

## 1 | INTRODUCTION

Magnesium (Mg) alloys are widely used in many fields due to their significant advantages, such as high strength/weight ratio, appropriate machinability, high thermal conductivity, and good electromagnetic shielding characteristics.<sup>[1]</sup> However, Mg is relatively weak in some properties such as corrosion resistance, strength, ductility, and hardness. These weaknesses limit the widespread application of Mg and its alloys. To enhance the mechanical properties of Mg-based materials,

nanocomposites have gained extensive attention from researchers in recent years. It has been shown that simultaneous enhancement in mechanical properties can be achieved by adding nano-sized reinforcements to the Mg matrix.<sup>[2–7]</sup>

Kamrani et al. reported that introducing SiC nanoparticles (SiC<sub>n</sub>) up to 10 vol% to the Mg matrix effectively enhances the strength and ductility of the Mg nanocomposites.<sup>[8–10]</sup> However, the improvement of mechanical properties is just one of the optimization procedures for the wide application of Mg-based materials. The

This is an open access article under the terms of the Creative Commons Attribution License, which permits use, distribution and reproduction in any medium, provided the original work is properly cited.

© 2022 The Authors. *Materials and Corrosion* published by Wiley-VCH GmbH.

corrosion susceptibility is especially important in Mg-SiC composites, where galvanic couples form between SiC particles and the Mg matrix due to different standard electrode potentials.<sup>[11,12]</sup> In the case of Al composites, some studies revealed that the SiC particles increase the corrosion rate of the composite as they act as a local cathode for galvanic corrosion.<sup>[13–15]</sup> It has been shown that the corrosion rate intensified as the size of the SiC particles increased.<sup>[15]</sup>

The coating is an effective method against corrosion and there are many different coating materials and methods, which can be employed. Effective coatings should be hard and stable with high adhesion to the substrate, otherwise, there is a high risk of galvanic corrosion in case of scratches and wear defects.<sup>[1]</sup>

Plasma electrolytic oxidation (PEO) is an effective method to apply coatings on Mg-based materials. It is based on the anodic oxidization of the metal substrate in a particular electrolyte under high potential. The formation mechanism of the PEO coating is based on the following steps: (a) high voltage provides the required energy for current to flow through a small area of the surface locally, and (b) a plasma environment forms in which arises a very high temperature of over 1000°C, (c) the substrate locally melts and reacts with the components inside the electrolyte, (d) the reaction products rapidly solidify and a crater (discharge channel) forms locally on the surface,<sup>[16]</sup> (e) a small part of the PEO coating forms locally around the craters.<sup>[17,18]</sup> The PEO oxide layer is hard, stable, and bonded strongly to the substrate.<sup>[19–21]</sup> The electrolytes are environmentally friendly, and the process requires little or no pretreatment. The PEO coating is typically composed of two layers; an outer porous layer and an inner barrier film, which can effectively resist corrosion.<sup>[22]</sup>

The impressive effect of the PEO coating on the general corrosion and tribological behavior of Mg-based materials is documented in the literature.<sup>[23–25]</sup> Several studies have been done to investigate the corrosion behavior of PEO coating on Mg through different electrochemical methods such as polarization and electrochemical impedance spectroscopy (EIS).<sup>[26–31]</sup> However, not many studies have been performed on the corrosion behavior of Mg composites, where galvanic corrosion is the dominant corrosion mechanism because of the reinforcement particles.<sup>[16,32–36]</sup> The volume fraction of reinforcement particles in a composite is a parameter that can affect the corrosion behavior of materials due to the accumulation of internal stress, grain refining, and cell structure formation.<sup>[37]</sup> However, the effect of volume fraction of reinforcements on microstructure and corrosion behavior of composite materials have been rarely investigated.<sup>[37,38]</sup>

Here, we investigated the following main topics: (a) the coating structure of the PEO coating on Mg nanocomposites, (b) the influence of SiC nanoparticles on the protection ability of the PEO coating, and (c) the galvanic corrosion process occurring between Mg matrix and SiC particles. Based on the corrosion test results, the presence of SiC<sub>n</sub> nanoparticles up to a specific amount positively influences the coating formation process and corrosion behavior of the Mg substrate coated with the PEO oxide layer. A higher percentage of the SiC nanoparticles in the substrate leads to the formation of a thinner coating layer, which is more porous and contains more microcracks compared to the coating on the sample with a lower percentage of SiC nanoparticles.

## 2 | EXPERIMENTAL METHODS

### 2.1 | Composite manufacturing

Mg powder with an average particle size of –325 mesh and SiC<sub>n</sub> particles (Alfa Aesar, Ward Hill) with an average particle size of 50 nm were used to fabricate the Mg-SiC nanocomposite. Mg powders with additions of 1, 3, and 10 vol% of SiC<sub>n</sub> particles were mechanically milled up to 25 h to produce M1Sn, M3Sn, and M10Sn samples, respectively. The milled composite powders were cold isostatically pressed at a pressure of 700 MPa with a holding time of 10 min, sintered at 600°C for 2 h in an argon atmosphere, and further densified through hot extrusion at 400°C with a press ratio of 22:1. The cylindrical specimens with a diameter of 5 mm and a height of 10 mm were cut in the extrusion direction by wire electric discharge machining (EDM, GF Agie Charmilles). The surfaces were polished down to 1 μm to remove the oxide and EDM-induced damage surface and to generate smooth surfaces. As a reference, pure Mg powders, named MM, were processed by the same processing steps. More detailed information regarding the manufacturing process is given in Kamrani et al.,<sup>[8]</sup> Ghasemi et al.,<sup>[9]</sup> and Penther et al.<sup>[10]</sup>

### 2.2 | Coating process

For PEO, the samples were connected as an anode while immersed in a silicate-based electrolyte with 10 g/l Na<sub>2</sub>SiO<sub>3</sub> and 10 g/l KOH in water. A stainless-steel plate was used as a cathode. To start the process, a high voltage of about 300 V with pulsed DC was applied by using the AXD compact power supply of Munk company. The temperature and agitation of the electrolyte were kept constant at 25°C and 200 revs/min, respectively. The

samples were processed for 5 min and about three samples were coated for each case.

### 2.3 | Coating characterization

The morphology and thickness of the PEO coatings were characterized using high-resolution scanning electron microscopy (HRSEM, Gemini 500). Elemental analysis was performed by energy-dispersive X-ray spectrometry (EDX, Bruker Quantax Berlin) attached to the HRSEM. XRD was performed with a Bruker D8 diffractometer to investigate the role of SiC on the structure of the nanocomposites as well as on the PEO coatings. For this purpose, a Cu  $K_{\alpha}$  radiation source and a Lynxeye detector were used under a locked coupled 2-theta scan type and continuous scan mode with a 2-theta rotating angle from  $2^{\circ}$  to  $90^{\circ}$ . The pattern has been indexed by the original JCPDS data of the XRD peaks characteristic. The Rietveld software, MAUD 2.79, has been employed to analyze all the diffraction results.

The elements and chemical species of the samples were characterized layer by layer from the uppermost surface of the coating toward the depth of the substrate within 151 etching steps with X-ray photoelectron spectroscopy (XPS; ThermoScientific). The Al  $K_{\alpha}$  radiation was used as an X-ray source, and the photoelectron take-off angle was set at  $45^{\circ}$ . Because of a thin layer of organic elements on the surface, the first etching layer was neglected. The deconvolution of the overlapped XPS peaks was performed using the Peak Fit module provided with Gram-Charlier A Series (GCAS) function.

### 2.4 | Corrosion evaluation

To evaluate the corrosion behavior, at least three coated samples of each case with a similar condition were tested in a 3.5% NaCl solution at room temperature through

EIS and potentiodynamic polarization tests. The tests were conducted with a potentiostat device (Voltalab PGZ 402) from Radiometer Analytical SAS company. The EIS test was carried out using a standard three-electrode corrosion cell with a volume of about  $450\text{ cm}^3$  which consisted of a saturated calomel electrode (SCE—3 mol/l KCl) reference electrode, a platinum counter electrode, and a working electrode or test specimen. The EIS experiment was performed in the frequency range between 0.01 and  $10^5\text{ Hz}$  with an AC voltage amplitude of 10 mV. The EIS data were analyzed by curve fitting and equivalent circuit modeling using ZView electrochemical analysis software. Potentiodynamic polarization curves were acquired at a scan rate of  $2.5\text{ mV}\cdot\text{s}^{-1}$  from  $-2000$  to 0 mV. The  $E_{\text{corr}}$  and  $I_{\text{corr}}$  were obtained using the Tafel extrapolation method and the open-circuit potential (OCP) was directly obtained from Tafel curves.

## 3 | RESULTS

### 3.1 | Microstructure of the composite and coating structure

Figure 1 shows the microstructure of the M1Sn and M10Sn which demonstrate the uniform distribution of the SiC nanoparticle in the Mg matrix. The influence of embedded SiC nanoparticles on the structure of the PEO coatings was investigated by SEM analysis. Figure 2 demonstrates the surface morphology of the PEO-coatings on the MM, M1Sn, and M10Sn composites samples. The surface of the PEO-treated samples exhibits the typical porous feature of the PEO coatings with many pores that are homogeneously distributed over the surface. In the MM and M1Sn samples, the PEO layer contains many round pores on the micron scale.

The coating on the M10Sn specimen represents relatively smaller pores that are uniformly distributed

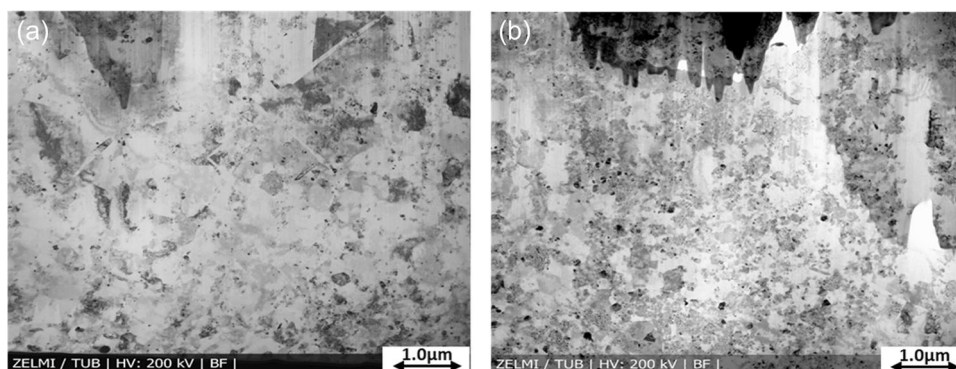
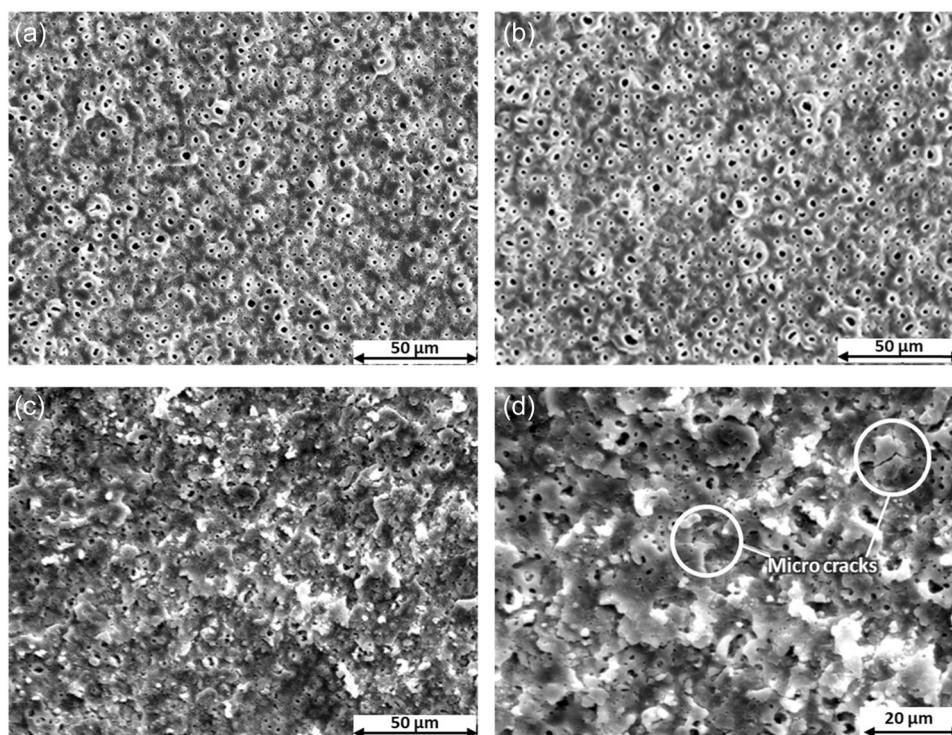


FIGURE 1 TEM images regarding the microstructure of the nanocomposite samples: (a) M1Sn and (b) M10Sn



**FIGURE 2** Surface morphology of the plasma electrolytic oxidation (PEO) coatings on nanocomposite samples: (a) MM, (b) M1Sn, (c, d) M10Sn in different magnification

on the surface. The higher volume percentage of  $\text{SiC}_n$  nanoparticles in the M10Sn samples leads to the formation of different surface morphology of the PEO coating. Here, the coating surface is rougher and the pores are finer compared to those of the MM and M1Sn samples. Figure 2d shows the surface morphology of PEO coating on M10Sn in higher magnification. The surface of the coating contains microcracks and it is quite uneven and rough.

The cross-sections of the MM, M1Sn, M3Sn, and M10Sn coatings can be seen in Figure 3. The bright particles that can be seen in the substrates of MM, M1Sn, M3Sn, and M10Sn, indicate the uniform distribution of the SiC nanoparticles in the Mg composite and no agglomeration. The typical cross-section of PEO coatings indicates that the coating layer on M10Sn is thinner compared to those of the MM and M1Sn. The thickness of the PEO layer on MM and M1Sn samples which is an average from five different measurements is about  $4 \pm 1 \mu\text{m}$ , that of M3Sn is about  $3 \pm 0.7 \mu\text{m}$  and that of the M10Sn is about  $2 \pm 0.5 \mu\text{m}$ .

The cross-section of the M10Sn specimen illustrates a different coating structure compared to those of MM and M1Sn. The structure of M10Sn is finer, smaller, and is composed of more pores compared to MM and M1Sn. By higher magnification in Figure 3d, it is seen that the oxide coating cross-section contains pores and all PEO

coatings are composed of two layers; an outer porous layer on the top and a very thin inner barrier layer in direct contact and bound to the substrate.

Figure 4 shows the chemical composition of the PEO coating on the M10Sn determined by EDX analysis along the line AB. Point A is located deep in the substrate, and point B is located on the coating surface. The chemical composition of point A shows a higher amount of Mg but a lower amount of O and Si. Moving from point A to B, the Mg curve decreases suddenly by reaching the interface between coating and substrate. Simultaneously, O and Si curves rise rapidly. The change of the chemical composition over the coating/substrate interface indicates the formation of a layer on the surface. Compared to the substrate, more O and Si and lower amounts of Mg are detected in the coating area. Detection of high C content on the uppermost layer of coating can be related to contaminations and impurities on the surface. The EDX results suggest the presence of  $\text{Mg}_2\text{SiO}_4$  and MgO in the coatings.

### 3.2 | Phase identification

Figure 5 illustrates the XRD patterns of the coated MM, M1Sn, and M10Sn specimens. Mg, MgO, and  $\text{Mg}_2\text{SiO}_4$  are detected in all samples. The SiC peaks could be

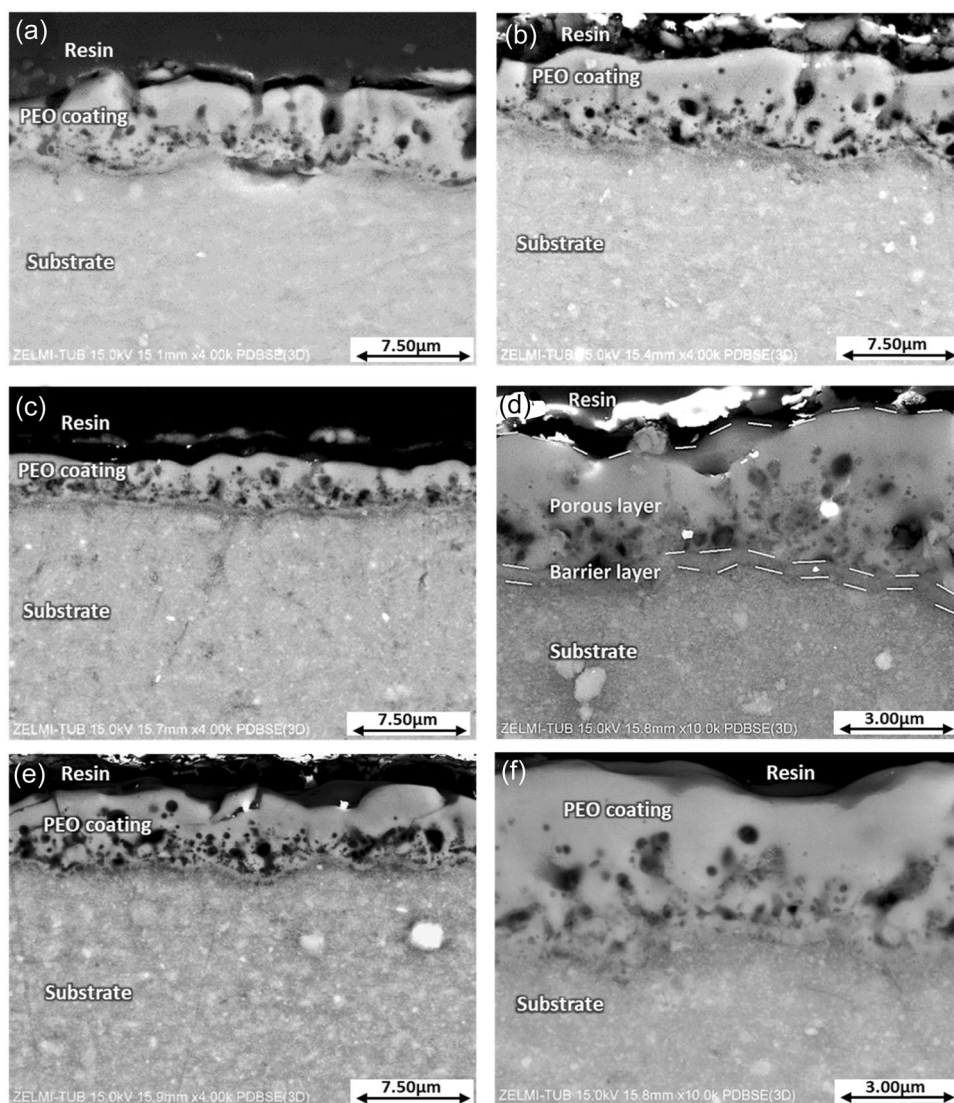


**FIGURE 3** Backscattered SEM images from a cross-section of plasma electrolytic oxidation (PEO) coatings: (a) MM, (b) M1Sn, (c, d) M10Sn (e, f) M3Sn

detected just in M1Sn and M10Sn samples. As the penetration depth of the X-ray beam is much greater than the coating thickness, the detection of SiC and Mg crystals can be related to the phases in the substrate and that of the MgO and Mg<sub>2</sub>SiO<sub>4</sub> to the oxide compounds forming in the coating layer on the surface.

### 3.3 | Coating analysis

The fitted spectra in Figure 6 show the XPS patterns of PEO layers and corresponding substrate. The patterns are related to high-resolution spectra of O 1s, C 1s, Si 2p, and Mg 1s-KLL resulting from 150 etching levels from the coating surface toward the substrate of MM, M1Sn, and M10Sn samples. According to the XPS spectra, the major surface elements existing in the specimens are Si, O, C, and Mg.

In the case of Si 2P, two peaks with a binding energy of 101.8 and 99.7 eV are detected. The intensity of both peaks changes as it moves from the free surface of the coating (etching level = 0) toward the substrate (etching level = 150) for all samples namely MM, M1Sn, and M10Sn samples. The 101.8 peak has a high intensity in the lower etching levels, and its intensity gets lower and lower as the etching process proceeds. Based on the XPS database,<sup>[39,40]</sup> the 101.8 peak represents the Mg<sub>2</sub>SiO<sub>4</sub>. The 101.8 peaks disappear as the etching process reaches about 79th, 75th, and 60th of etching levels for MM, M1Sn, and M10Sn, respectively.

The peak with 99.7 eV emerges with low and ascending intensity at the etching levels, where the 101.8 peak disappears. The 99.7 peak is a combination of Si (99.6 eV) and SiC (100.3 eV).<sup>[39,40]</sup> Opposite to the Si peak (99.6 eV), which exists in all three samples, the SiC peak (100.3 eV) does not appear in the MM sample.

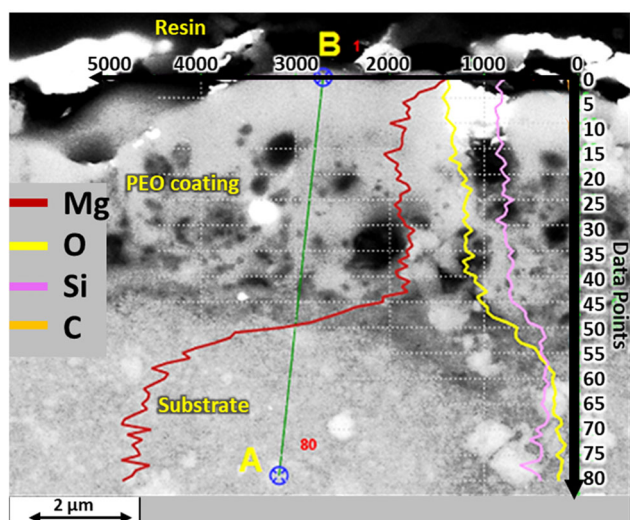


FIGURE 4 Energy-dispersive X-ray spectrometry line scan in the cross-section of M10Sn plasma electrolytic oxidation coatings.

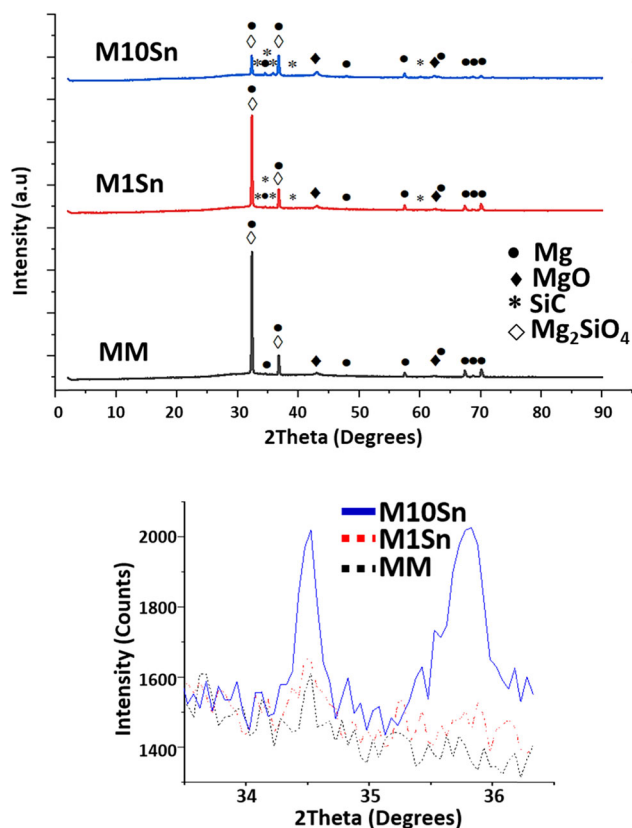


FIGURE 5 Representative diffractograms of MM, M1Sn, and M10Sn coated samples with a magnified view of the SiC peaks in the range of  $34^{\circ}$ – $36^{\circ}$

In the case of (C 1 s) patterns, no apparent peak can be seen in the first 60 etching steps in all samples. However, the peak of 283.5 eV, which can be related to the SiC, appears from the 75th and 60th levels of etching

in M1Sn and M10Sn, respectively. This data confirms the presence of SiC reinforcement particles in the nanocomposite substrate of M1Sn and M10Sn samples.

In the patterns of Mg 1 s KLL, a peak with 306.0 eV can be seen, which, based on the XPS database, can be related to MgO. This peak shows a slight descending trend as the etching process proceeds from the coating surface to the substrate. Two other peaks, namely those with 301.1 and 311.8 eV represent Mg metal-binding energy and appear with a sharp ascending slope from 79th, 75th, and 60th levels of etching in MM, M1Sn, and M10Sn, respectively.

In the case of O 1S, one peak with a binding energy of 531.2 eV was detected. This peak is composed of two subpeaks, namely  $Mg_2SiO_4$  (530.1 eV) and MgO (531.0 eV).<sup>[39,40]</sup> The 531.2 peak has a high intensity at the beginning of the etching process (etching level = 0). The intensity remains almost constant until it reaches about 79th, 75th, and 60th of etching levels for the MM, M1Sn, and M10Sn, respectively. After that, the intensity of the peaks gradually decreases due to the absence of the  $Mg_2SiO_4$  in the substrate area (Figure 7). The peak with a binding energy of 531.0 eV (MgO) remains in the pattern up to the final etching level of 150.

### 3.4 | Corrosion tests

Figure 8 demonstrates the potentiodynamic polarization curves of the samples. The corrosion results of the M3Sn sample are also inserted here to understand better the influence of the reinforcement particle and its volume fraction on the corrosion behavior of the coatings. The corresponding data derived from the curves are summarized in Table 1. The corrosion current densities ( $I_{corr}$ ) for MM, M1Sn, M3Sn, and M10Sn are about 0.9261, 0.5279, 0.9778, and 4.1208 ( $\mu A/cm^2$ ), respectively. The corresponding corrosion rates of the samples are 19.49, 11.11, 20.57, and 86.72 mils per year (m/Y), respectively. The M1Sn has the lowest current density ( $I_{corr}$ ), therefore it has the highest corrosion resistance compared to MM, M3Sn, and M10Sn samples. The corrosion rates of MM and M3Sn samples are comparable and lower than that of the M10Sn. The highest corrosion rate belongs to the M10Sn sample.

The  $E_{corr}$  shows a relation with the volume percentage of SiC<sub>n</sub> nanoparticles so that the higher percentage of nanoparticles leads to nobler  $E_{corr}$ . The MM curve with a corrosion current density of about 0.9261  $\mu A/cm^2$  is on the most left side of the diagram with the less noble corrosion potential. In the case of the M1Sn sample with the lowest corrosion resistance, the corrosion potential is less noble than M10Sn and nobler than MM. In general,

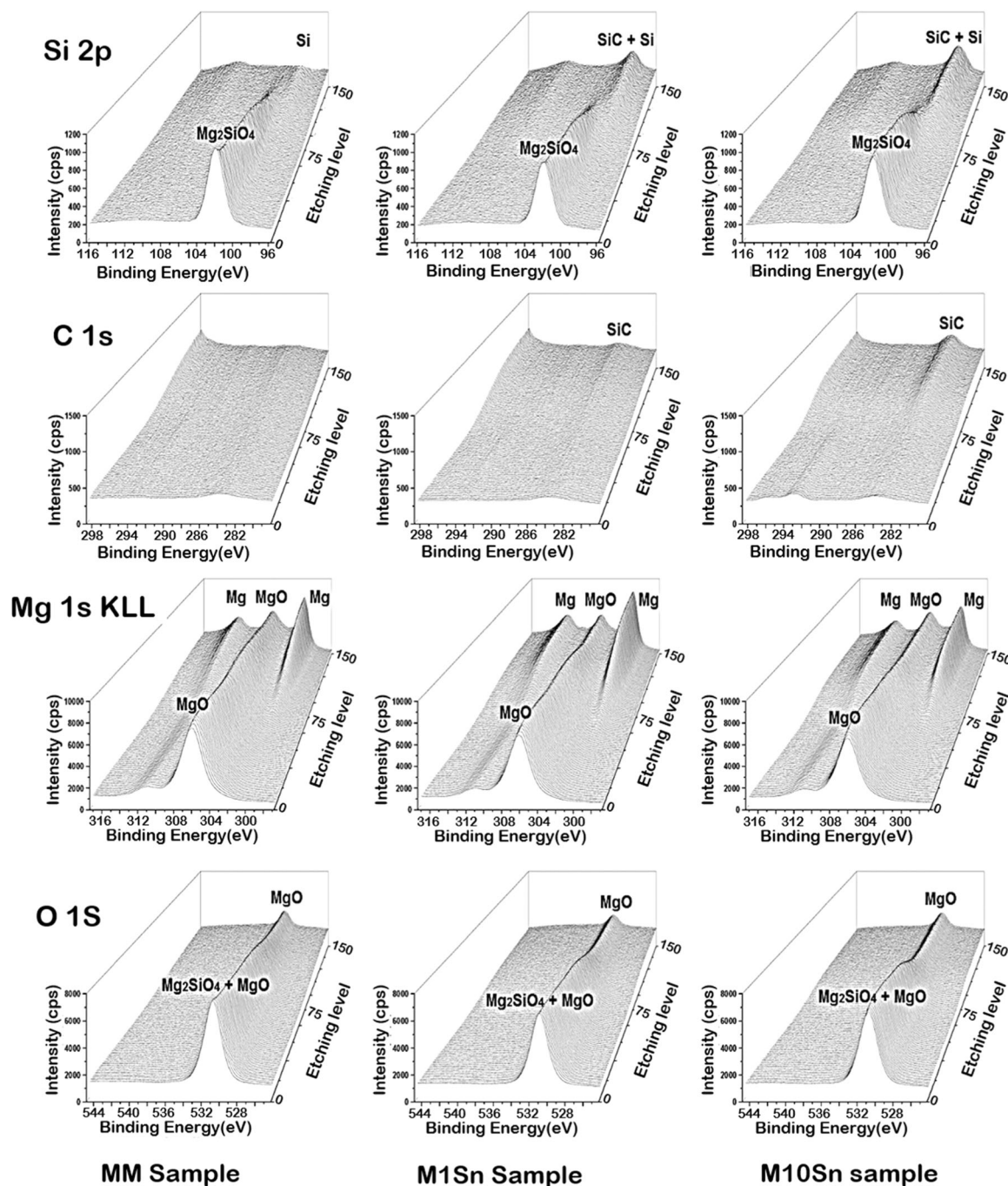


**FIGURE 6** X-ray photoelectron spectroscopy spectra of plasma electrolytic oxidation layers on MM, M1Sn, and M10Sn samples from the free surface of the coating (etching level = 0) toward the substrate (etching level = 150)

the  $I_{\text{corr}}$  shift to higher amounts as a higher volume percentage of SiC particles is used. This results subsequently in the different corrosion rates of the samples as follows  $\text{M10Sn} > \text{M3Sn} > \text{MM} > \text{M1Sn}$ .

The corrosion behavior of the coated samples was studied by EIS to achieve the corresponding impedance spectra. The impedance spectra are mainly characterized by double capacitive loops (two semicircles) in all specimens. The obtained data were fitted to semicircle

Nyquist curves and are depicted in Figure 9. The results show that the Nyquist curve of the M1Sn has a greater diameter than other samples, which can be attributed to higher corrosion resistance and more stability of the PEO coating. On the contrary, the Nyquist curves of the M3Sn and M10Sn samples are smaller, which means lower corrosion resistance of the corresponding coatings.

In the case of M3Sn and M10Sn, the capacitive loop appears at the lowest frequency ranges (at the end of the

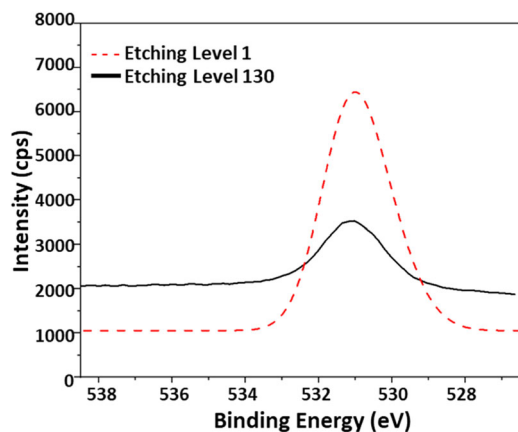


FIGURE 7 O 1s core-level X-ray photoelectron spectroscopy spectra for sample M10Sn at etching levels 1 and 130

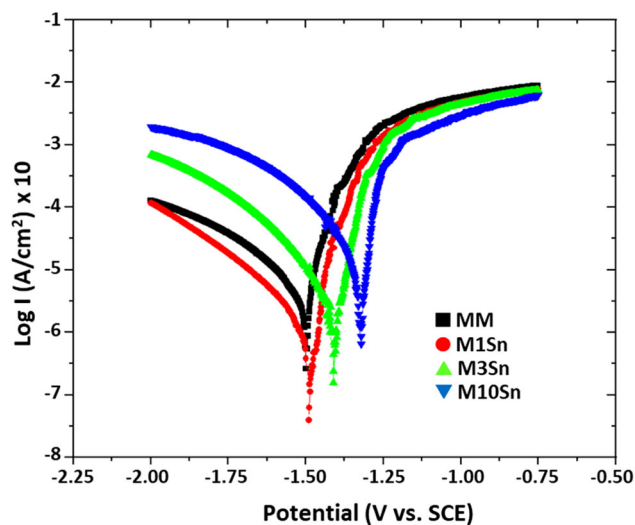


FIGURE 8 Polarization curves of MM, M1Sn, M3Sn, M10Sn in 3.5 wt.% NaCl aqueous solution at 25°C.

TABLE 1 The results of potentiodynamic polarization tests for MM, M1Sn, M3Sn, and M10Sn

Material	$E_{corr}$ (mV/SCE)	$I_{corr}$ ( $\mu\text{A}/\text{cm}^2$ )	$R_p$ ( $\text{k}\Omega \cdot \text{cm}^2$ )	CR (m/Y)
MM	-1501.2	0.9261	5.48	19.49
M1Sn	-1493.9	0.5279	34.47	11.11
M3Sn	-1414.3	0.9778	8.49	20.57
M10Sn	-1327.8	4.1208	2.43	86.72

curves), while MM forms an inductive loop. In other words, the M3Sn and M10Sn illustrate similar corrosion behavior, which is different from those of MM and M1Sn. The latter results are in good agreement with Tafel curves, and the results obtained from potentiodynamic tests (Figure 8).

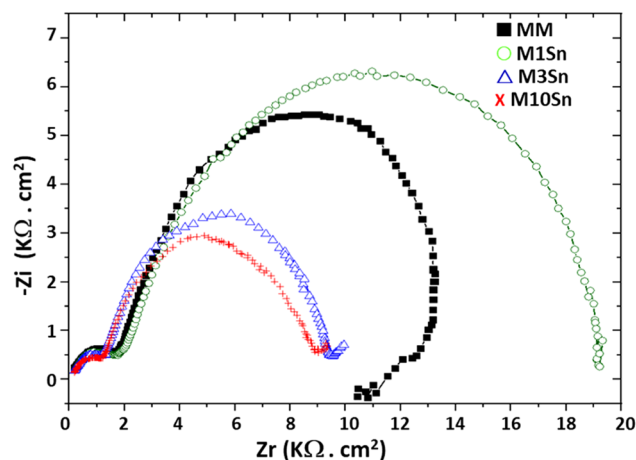


FIGURE 9 Electrochemical impedance spectroscopy (EIS) curves of the MM, M1Sn, M3Sn, and M10Sn at the open circuit potential from the electrochemical EIS in 3.5 Wt.% NaCl solution at 25°C

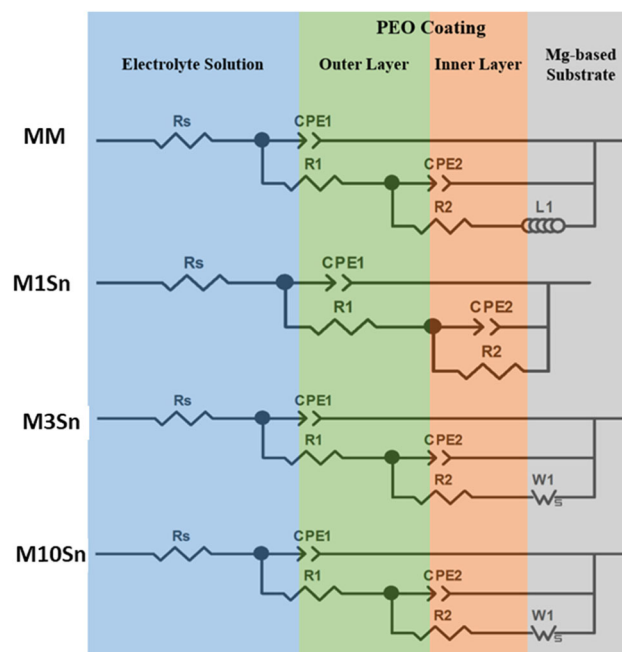


FIGURE 10 The proposed equivalent electrical circuit used for modeling impedance spectra of plasma electrolytic oxidation-coated Mg samples with and without  $\text{SiC}_n$  nanoparticles

To understand the corrosion mechanism and parameters controlling the corrosion reactions, the impedance spectra of each sample were modeled and fitted to the equivalent circuits (Figure 10). The best-fitting data for the MM sample without  $\text{SiC}_n$  nanoparticles results from an equivalent circuit composed of capacitors, resistors, and one inductor. In the circuits, the resistor  $R_s$  relates to the solution resistance, which is in series with a combination of constant

phase elements (CPEs) and other resistors reflecting the behavior of two different layers in the PEO coating. CPE simulates the behavior of a not ideal capacitor in a coating layer system whose capacitance changes depending on frequency. It reflects conditions and behavior of the sample, such as surface roughness and porosity, distribution of potential and current in the electrode, and the distributed surface reactivity of microscopic inhomogeneity in the coatings.<sup>[41,42]</sup>

For the M1Sn sample, the equivalent circuits are composed of just capacitors and resistors. For the samples with a higher amount of SiC nanoparticles, namely M3Sn and M10Sn, however, the best fitting data result from equivalent circuits composed of capacitors, resistors, and a Warburg—short circuit terminus element. A Warburg element clarifies the diffusion effects in the circuit between the inner layer of the PEO coating and the substrate.<sup>[43]</sup>

Table 2 represents the fitted parameters for the EIS spectra. Based on the EIS data, the highest resistance of the coating belongs to M1Sn, and a higher volume fraction of SiC deteriorates the corrosion resistance of the coatings in the case of M3Sn and M10Sn.

Figure 11 shows the Bode plots derived from the EIS method. The Bode diagrams display higher impedance values for M1Sn (4.3  $\Omega$ ) and MM (4.1  $\Omega$ ) compared to those of M3Sn (4.0  $\Omega$ ) and M10Sn (3.9  $\Omega$ ). The impedance values are confirming that the most effective barrier layer forms in the M1Sn coating. The impedance modulus ( $Z$ ) of all samples continually decreases, which indicates deterioration of the barrier layer as the immersion process proceeds. As can be seen, the outcomes of the Bode plots are in good agreement with the Nyquist curves and show the same trend of corrosion resistance for the samples. Here, the data corresponding to the low-frequency (<100 Hz) reflect the charge transfer behavior of the inner layer. On the contrary, the high range of the frequency (>1000 Hz) reflects the corrosion behavior of the outer porous layer.<sup>[44]</sup>

## 4 | DISCUSSION

### 4.1 | SEM, XRD, and EDX

The formation of PEO coatings with a comparable thickness on both, MM and M1Sn samples indicates that the presence of 1 vol% of SiC<sub>n</sub> nanoparticle leaves no negative influence on coating formation. However, addition of higher percentages of SiC namely 3 and 10 vol% deteriorates the coating formation process and

TABLE 2 Fitted parameters for the electrochemical impedance spectroscopy spectra depicted in Figure 9

Sample	$R_s$ ( $\Omega$ cm <sup>2</sup> )	CPE1-P ( $\Omega^{-1}$ cm <sup>-2</sup> s <sup>-1</sup> E-8)	CPE1-P (0.85 ± 0.03)	R1 ( $\Omega$ cm <sup>2</sup> )	CPE2-T ( $\Omega^{-1}$ cm <sup>-2</sup> s <sup>-1</sup> E-6)	CPE2-P (0.63 ± 0.01)	R2 ( $\Omega$ cm <sup>2</sup> )	W1-R ( $\Omega$ cm <sup>2</sup> )	W1-T ( $\Omega^{-1}$ cm <sup>-2</sup> )	W1-P	L1 (H cm <sup>2</sup> )	$\chi^2$ (x 10 <sup>-3</sup> )
MM	129.7 ± 18.8	4.1E ± 1.2	0.85 ± 0.03	1516 ± 61	7.61 ± 0.50	0.63 ± 0.01	13889 ± 310	-	-	-	259 ± 23	9.0
M1Sn	136.5 ± 7.7	15.6 ± 1.7	0.76 ± 0.01	1809 ± 27	3.49 ± 0.08	0.79 ± 0.01	17725 ± 125	-	-	-	-	2.3
M3Sn	109.5 ± 7.6	13.1 ± 1.8	0.78 ± 0.01	1325 ± 25	1.83 ± 0.08	0.85 ± 0.01	8151 ± 86	30E3 ± 496	177 ± 3.6	0.8 ± 0.1	-	3.1
M10Sn	102.3 ± 4.3	35.1 ± 3.1	0.72 ± 0.01	1283 ± 18	3.08 ± 0.11	0.83 ± 0.01	7370 ± 111	1342 ± 590	5.5 ± 4.8	0.5 ± 0.1	-	1.1

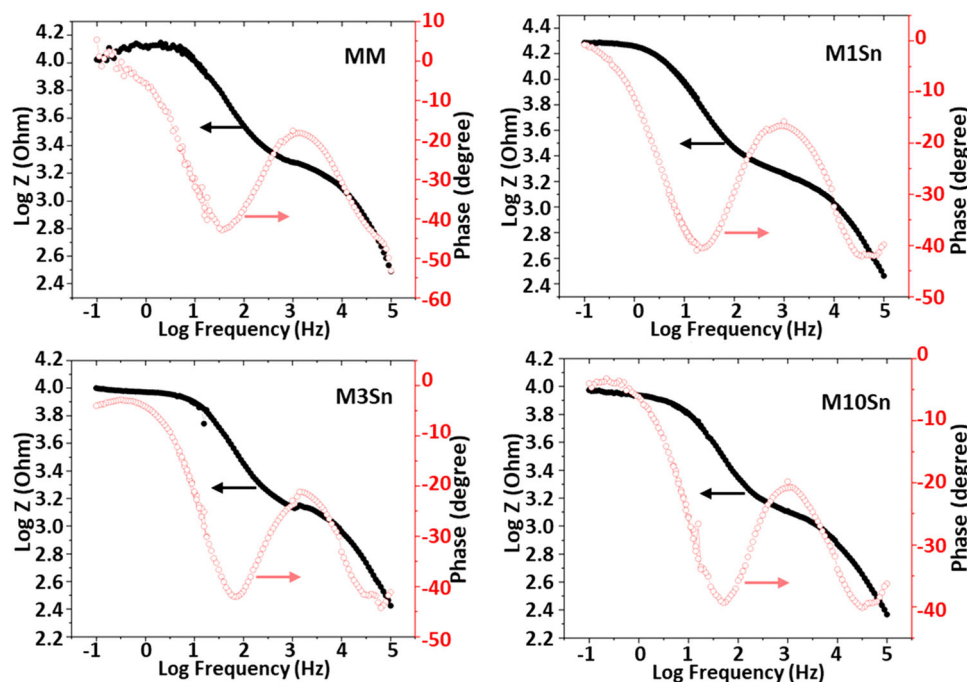


FIGURE 11 Bode-impedance (black solid circles) and bode-phase (red hollow circle) graphs of the plasma electrolytic oxidation coating on MM, M1Sn, M3Sn, and M10Sn in 3.5 wt.% NaCl solution

lower the thickness of the PEO coatings forms on the substrate.

The XRD results indicate peaks of Mg, MgO, and Mg<sub>2</sub>SiO<sub>4</sub> in the samples, which is in good agreement with previous studies.<sup>[8–10,16,19]</sup> The SEM/EDX results revealed that a higher amount of SiC<sub>n</sub> nanoparticles in the substrate influences the coating formation process negatively and leads to a thinner and rougher layer with fine pores and micro-cracks. The formation of a thinner layer on the sample with a higher volume fraction of SiC nanoparticles can be attributed to the higher melting point of the SiC<sub>n</sub> particles as a hard and stable ceramic material. The melting point of Mg is around 750°C, and that of the SiC<sub>n</sub> lies in the range of 2730°C.<sup>[45]</sup> The presence of a higher amount of SiC<sub>n</sub> nanoparticles in the substrate requires higher thermal energy to melt the substrate elements. As a higher amount of thermal energy gets absorbed by SiC<sub>n</sub> nanoparticles, the lower volume of the Mg melts. The latter effect leads to the formation of a thinner coating layer with smaller discharge channels. As the lower amount of the substrate converts to melt, it solidifies relatively faster compared to what happens by the M1Sn sample with 1 vol% SiC<sub>n</sub>. In M1Sn samples, a higher volume of the substrate gets melted, and the solidification time is longer compared to the M10Sn sample. The fast rate of solidification leads to high thermal stress and the formation of a rough and flaky surface full of microcracks in the coating structure of M10Sn.

## 4.2 | XPS

The XPS results of the Si 2p reveal that the intensity of the Mg<sub>2</sub>SiO<sub>4</sub> peaks decreases and the peaks disappear as it reaches the coating/substrate interface. The Si in the coating can originate from the SiC particles in the substrate and/or from SiO<sub>3</sub><sup>2-</sup> ions in the electrolyte. Considering the C 1s profiles, no evidence for the existence of C elements can be seen in the coating area. It reveals that no SiC particle has been transferred to the coating during the layer formation process. Therefore, the formation of Mg<sub>2</sub>SiO<sub>4</sub> can be related to SiO<sub>3</sub><sup>2-</sup> ions originating from the electrolyte. The SiC nanoparticles do not contribute to the coating formation and act as a barrier against the coating formation because of their high melting point. The PEO coating formation process is due to plasma formation, local melting, and rapid solidification. Therefore, a higher volume fraction of the SiC<sub>n</sub> nanoparticles with a high melting point can explain the formation of a thinner layer in M10Sn samples compared to those of MM and M1Sn.

The XPS results indicate the existence of the oxide phases in the substrate, which can be related to the MgO forming during the ball milling process during the production of the nanocomposite.<sup>[46]</sup> The XPS spectra reveal that pure Mg peaks just emerge as the etching process reaches the substrate. From the corrosion mechanism point of view, this is an important result as it shows that no pure Mg exists in the PEO coating,

which is only composed of hard and stable oxide compounds.

### 4.3 | Corrosion tests

The EIS tests result in the spectra which are mainly characterized by double capacitive loops (two semicircles). The high-frequency range of the EIS spectra is related to the reactions, processes, and microstructure of the outer layer. In contrast, the low-frequency range reveals the corrosion properties of the inner layers.<sup>[44]</sup> The small capacitance loop of samples in the higher frequency ranges corresponds to the fast charge-discharge process and a film effect. In contrast, the bigger capacitance loops indicate the relaxation of the electrical double layer.<sup>[47]</sup> These capacitive loops are originating from oxide (MgO), or hydroxide (Mg(OH)<sub>2</sub>) compounds forming quickly on the surface adjacent to the electrolyte.<sup>[48]</sup>

The potentiodynamic polarization results and EIS experiments revealed that the presence of about 1 vol% SiC<sub>n</sub> in the substrate has a positive influence on the corrosion behavior of the PEO coating compared to samples with 3 or 10 vol% SiC<sub>n</sub>. The relatively poor corrosion resistance of the M3Sn and M10Sn coatings can be related to the thinner PEO layers on the substrate due to the higher melting point of SiC nanoparticles hindering the coating formation process. It can also explain the formation of the pores and microcracks in the coating structure, which additionally deteriorate the corrosion resistance of the coating. The microcracks and cavities provide more penetration paths for the electrolyte solution toward the dense internal layer.<sup>[49]</sup>

According to the equivalent circuit results, the total corrosion resistance of the PEO coating can be related to three different layers resisting the charge transfer. The first layer is a porous layer on the top of the PEO coating, directly contacting the electrolyte. The combination of both CPE1 and R1 in parallel reflects the behavior of the outer layer of the PEO coating. On the contrary, the inner layer is a compact and stable layer that is directly bonded to the substrate. The behavior of the inner layer can be analyzed by corresponding data of CPE2 and R2 (charge transfer resistance) in parallel. The third layer is a Helmholtz double layer which forms when the inner layer breaks down.<sup>[23–25]</sup>

Based on the results, the outer layer of all samples shows a relatively lower value of resistance (R1) and capacitance (CPE1) compared to those of the inner layer (R2) and (CPE2). The outer layer of the PEO coating acts as a weak barrier against charge transfer, providing no effective corrosion resistance due to the high number of porosities and discharge channels. However, the inner

layer with a relatively high resistance value acts as an effective barrier layer against charge transfer and can protect the substrate against corrosion. The third layer comes into being when the inner layer finally fails and lets the corrosive solution pass through and come in direct contact with the substrate. At this moment, the arrangement of positive and negative charges on the surface leads to the formation of a double layer, which resists the charge transfer. The charge transfer behavior at the inner layer/substrate interface is different for MM, M1Sn, M3Sn, and M10Sn samples.

In the case of the MM sample, an inductive loop forms at low frequencies of the Nyquist curve, which can be related to pitting formation. Such corrosion behavior happens as the aggressive ions such as Cl<sup>-</sup> or H<sup>+</sup> concentrate on a local point. The high concentration of ions leads to pitting which happens based on the local corrosion mechanisms.<sup>[50,51]</sup> The inductive loop indicates that the aggressive agents or electron-accepting species had already reached the substrate and the dissolution process is going on. The corrosion products such as Mg<sup>2+</sup> are forming, and more species adsorb to the local defects leading to the pitting corrosion of Mg. The presence of an inductive element (L1) in the equivalent circuit also confirms the occurrence of the pitting corrosion on the bottom of the pores where the electrolyte reaches the Mg substrate.<sup>[52,53]</sup>

In the M3Sn and M10Sn samples, a capacitive loop can be seen at low frequencies of the Nyquist curve, which is simulated through the Warburg element (W1) in the equivalent circuit. The capacitive loops indicate the occurrence of diffusion-controlled kinetics, that is, mass transport through a corrosion product layer.<sup>[54]</sup> The latter effect takes place as the substrate is highly corroded and destroyed due to the porous nature of the PEO coatings. It is the moment when the coating fails and cannot protect the substrate anymore. The substrate provides enough electrons, which can be taken by electron-accepting species in the electrolyte. Under this condition, the electron consumer species are less than electrons that are available on the surface. Therefore, the corrosion process is controlled by the diffusion process, in which the electron-accepting species diffuse from the bulk of the electrolytes to the metal surface.

## 5 | CONCLUSION

The Mg nanocomposites samples with different volume fractions of SiC nanoparticles and the reference samples without SiC nanoparticles were prepared through mechanical milling and hot extrusion. All the samples were subsequently coated by the PEO process. The effect of the

volume fraction of SiC nanoparticles on corrosion properties of the PEO coating has been investigated. The following points can be concluded from the results.

- The results reveal that a higher percentage of the SiC nanoparticles in the substrate deteriorates the formation process of the PEO coating. It leads to the formation of a thinner coating layer that is more porous and contains more microcracks compared to the coating on the sample with a lower percentage of SiC nanoparticles.
- XPS and EDX experiments confirmed the presence of Mg<sub>2</sub>SiO<sub>4</sub> and MgO in the PEO layer, whereas SiC and Mg are detected only in the substrate. Based on the XPS observation, the SiC nanoparticles were not transferred to the coating during the layer formation process and no pure Mg exists in the PEO coating.
- Corrosion tests indicated that the presence of SiC<sub>n</sub> nanoparticles up to a specific amount in the substrate positively influences the corrosion behavior of the Mg substrate coated with the PEO oxide layer. Based on the corrosion results, PEO coating on Mg composite with 1 vol% SiC<sub>n</sub> particle shows better corrosion resistance compared to that of both samples without SiC and 3% or 10% SiC nanoparticle.

## ACKNOWLEDGMENTS

The authors gratefully acknowledge the financial support by the DFG (Deutsche Forschungsgemeinschaft) and the support by the members of the Non-Metallic Inorganic Materials group, Institute of Materials Science at TU Darmstadt for providing the ball mill equipment and research facilities. The authors further thank Daniela Hübler for sample production, Dr. Johannes Schmidt, Institute of Chemistry - Funktionsmaterialien (TU Berlin) for XRD and XPS analyses, Ulrich Gernert at the Central Electron Microscopy Unit (ZELMI) of TU Berlin for the SEM experiments and measurements and René Nitschke at the Extrusion Research and Development Center (FZS)—Metallic Materials at TU Berlin for the execution of the hot extrusion experiments. Open Access funding enabled and organized by Projekt DEAL.

## DATA AVAILABILITY STATEMENT

Research data are not shared.

## ORCID

Sepideh Kamrani  <http://orcid.org/0000-0003-0449-6085>

Alireza Ghasemi  <http://orcid.org/0000-0002-2614-5094>

## REFERENCES

- [1] K. J. Huang, H. G. Liu, C. R. Zhou, *Trans. Tech. Publ.* **2011**, 179-180, 757.
- [2] S. Kamrani, D. Hübler, A. Ghasemi, C. Fleck, *Materials* **2019**, *12*, 3445.
- [3] Q. Nguyen, M. Gupta, *J. Alloys Compd.* **2008**, *459*, 244.
- [4] C. Goh, J. Wei, L. Lee, M. Gupta, *Mater. Sci. Eng. A* **2006**, *423*, 153.
- [5] H. Dieringa, *J. Mater. Sci.* **2011**, *46*, 289.
- [6] E. Ghali, *Corrosion Resistance of Aluminum and Magnesium Alloys: Understanding, Performance, and Testing*, John Wiley & Sons, New York **2010**.
- [7] S. Sankaranarayanan, U. P. Nayak, R. Sabat, S. Suwas, A. Almajid, M. Gupta, *J. Alloys Compd.* **2014**, *615*, 211.
- [8] S. Kamrani, D. Penther, A. Ghasemi, R. Riedel, C. Fleck, *Adv. Powder Technol.* **2018**, *29*, 1742.
- [9] A. Ghasemi, D. Penther, S. Kamrani, *Mater. Charact.* **2018**, *142*, 137.
- [10] D. Penther, C. Fleck, A. Ghasemi, R. Riedel, S. Kamrani, *Key Eng. Mater. Trans. Tech. Publ.* **2017**, *742*, 165.
- [11] M. E. Turan, Y. Sun, Y. Akgul, *J. Alloys Compd.* **2018**, *740*, 1149.
- [12] S. Tiwari, R. Balasubramaniam, M. Gupta, *Corros. Sci.* **2007**, *49*, 711.
- [13] L. Diaz-Ballote, L. Veleza, M. Pech-Canul, M. Pech-Canul, D. O. Wipf, *J. Electrochem. Soc.* **2004**, *151*, B299.
- [14] A. Trowsdale, B. Noble, S. Harris, I. Gibbins, G. Thompson, G. Wood, *Corros. Sci.* **1996**, *38*, 177.
- [15] M. Montoya-Dávila, M. Pech-Canul, M. Pech-Canul, *Powder Technol.* **2009**, *195*, 196.
- [16] A. Pardo, S. Merino, M. Merino, I. Barroso, M. Mohedano, R. Arrabal, F. Viejo, *Corros. Sci.* **2009**, *51*, 841.
- [17] D.-S. Tsai, C.-C. Chou, *Metals* **2018**, *8*, 105.
- [18] T. Mi, B. Jiang, Z. Liu, L. Fan, *Electrochim. Acta* **2014**, *123*, 369.
- [19] A. Yerokhin, X. Nie, A. Leyland, A. Matthews, S. Dowe, *Surf. Coat. Technol.* **1999**, *122*, 73.
- [20] Y. Gao, A. Yerokhin, A. Matthews, *Surf. Coat. Technol.* **2013**, *234*, 132.
- [21] C. Blawert, W. Dietzel, E. Ghali, G. Song, *Adv. Eng. Mater.* **2006**, *8*, 511.
- [22] L.-L. Liu, P.-X. Yang, C.-N. Su, H.-F. Guo, M.-Z. An, *Int. J. Electrochem. Sci.* **2013**, *8*, 6077.
- [23] A. Ghasemi, V. Raja, C. Blawert, W. Dietzel, K. Kainer, *Surf. Coat. Technol.* **2008**, *202*, 3513.
- [24] A. Ghasemi, V. Raja, C. Blawert, W. Dietzel, K. Kainer, *Surf. Coat. Technol.* **2010**, *204*, 1469.
- [25] A. Ghasemi, N. Scharnagl, C. Blawert, W. Dietzel, K. Kainer, *Surf. Eng.* **2010**, *26*, 321.
- [26] Y. Gao, A. Yerokhin, A. Matthews, *Surf. Coat. Technol.* **2015**, *269*, 170.
- [27] J. Gao, X. Shi, B. Yang, S. Hou, E. Meng, F. Guan, S. Guan, *J. Mater. Sci. Mater. Med.* **2011**, *22*, 1681.
- [28] J. Gao, S. Guan, J. Chen, L. Wang, S. Zhu, J. Hu, Z. Ren, *Appl. Surf. Sci.* **2011**, *257*, 2231.
- [29] Y. Gu, S. Bandopadhyay, C.-F. Chen, C. Ning, Y. Guo, *Mater. Des.* **2013**, *46*, 66.
- [30] D. Sreekanth, N. Rameshbabu, *Mater. Lett.* **2012**, *68*, 439.
- [31] X. Yang, M. Li, X. Lin, L. Tan, G. Lan, L. Li, Q. Yin, H. Xia, Y. Zhang, K. Yang, *Surf. Coat. Technol.* **2013**, *233*, 65.
- [32] R. Lindström, L.-G. Johansson, G. E. Thompson, P. Skeldon, J.-E. Svensson, *Corros. Sci.* **2004**, *46*, 1141.

- [33] L. Cui, L. Xiaogang, *Rare Met.* **2006**, *25*, 190.
- [34] R. Lindström, L. G. Johansson, J. E. Svensson, *Mater. Corros.* **2003**, *54*, 587.
- [35] R. Lindström, J.-E. Svensson, L.-G. Johansson, *J. Electrochem. Soc.* **2002**, *149*, B103.
- [36] W. Ferrando, *J. Mater. Eng.* **1989**, *11*, 299.
- [37] Z. R. Hesabi, A. Simchi, S. S. Reihani, *Mater. Sci. Eng. A* **2006**, *428*, 159.
- [38] K. Ralston, N. Birbilis, *Corrosion* **2010**, *66*, 7500501.
- [39] L. Kang, J. Gao, H. Xu, S. Zhao, H. Chen, P. Wu, *J. Cryst. Grow.* **2006**, *297*, 100.
- [40] D. Veys-Renaux, E. Rocca, J. Martin, G. Henrion, *Electrochim. Acta* **2014**, *124*, 36.
- [41] K. M. Lee, K. R. Shin, S. Namgung, B. Yoo, D. H. Shin, *Surf. Coat. Technol.* **2011**, *205*, 3779.
- [42] M. Montemor, R. Pinto, M. Ferreira, *Electrochim. Acta* **2009**, *54*, 5179.
- [43] M. Sowa, W. Simka, *Surf. Coat. Technol.* **2018**, *344*, 121.
- [44] D. Chen, R. Wang, Z. Huang, Y. Wu, Y. Zhang, G. Wu, D. Li, C. Guo, G. Jiang, S. Yu, *Appl. Surf. Sci.* **2018**, *434*, 326.
- [45] P. Verma, P. Kumari, J. Ghose, V. Pandey, *Innovation in Materials Science and Engineering*, Springer, Singapore **2019**.
- [46] D. Penther, A. Ghasemi, R. Riedel, C. Fleck, S. Kamrani, *Mater. Sci. Eng. A* **2018**, *738*, 264.
- [47] M. Toorani, M. Aliofkhaezraei, A. S. Rouhaghdam, *Surf. Coat. Technol.* **2018**, *352*, 561.
- [48] Z. Shahri, S. Allahkaram, R. Soltani, H. Jafari, *Surf. Coat. Technol.* **2018**, *347*, 225.
- [49] H. Yu, Q. Dong, J. Dou, Y. Pan, C. Chen, *Appl. Surf. Sci.* **2016**, *388*, 114.
- [50] Y. Song, D. Shan, R. Chen, E.-H. Han, *Corros. Sci.* **2009**, *51*, 1087.
- [51] Z. Song, Z. Xie, G. Yu, B. Hu, X. He, X. Zhang, *J. Alloys Compd.* **2015**, *623*, 274.
- [52] L.-Y. Cui, S.-D. Gao, P.-P. Li, R.-C. Zeng, F. Zhang, S.-Q. Li, E.-H. Han, *Corros. Sci.* **2017**, *118*, 84.
- [53] T. S. Lim, H. S. Ryu, S.-H. Hong, *Corros. Sci.* **2012**, *62*, 104.
- [54] C. M. Brett, L. Dias, B. Trindade, R. Fischer, S. Mies, *Electrochim. Acta* **2006**, *51*, 1752.

**How to cite this article:** A. P. Golhin, S. Kamrani, C. Fleck, A. Ghasemi, *Mater. Corros.* **2022**;73:1813–1825.

<https://doi.org/10.1002/maco.202213118>